

# Lawrence Berkeley National Laboratory

## Recent Work

### Title

Phase State and Physical Properties of Ambient and Laboratory Generated Secondary Organic Aerosol

### Permalink

<https://escholarship.org/uc/item/81x7b8sk>

### Journal

Geophys. Res. Lett, 41

### Authors

O'Brien, Rachel E.  
Neu, Alexander  
Epstein, Scott A.  
et al.

### Publication Date

2014-08-31

**Draft 5 (GRL= 5 pages max)**

# **Phase State and Physical Properties of Ambient and Laboratory Generated Secondary Organic Aerosol**

**Rachel E. O'Brien,<sup>1,2\*</sup> Alexander Neu,<sup>1</sup> Scott A. Epstein,<sup>3</sup> Amanda C. MacMillan,<sup>3</sup> Sergey  
A. Nizkorodov,<sup>3</sup> Alexander Laskin,<sup>4</sup> Ryan C. Moffet,<sup>2</sup> Mary K. Gilles,<sup>1</sup>**

[1] Lawrence Berkeley National Laboratory, Berkeley, California, 94720-8198, USA

[2] Department of Chemistry, University of the Pacific, Stockton, CA 95211, USA

[3] Department of Chemistry, University of California, Irvine, CA 92697-2025, USA

[4] William R. Wiley Environmental and Molecular Sciences Laboratory, Pacific Northwest  
National Laboratory, Richland, WA, 99352, USA

\*Address correspondence to the following author

Email: resellon@lbl.gov

Address: Lawrence Berkeley National Lab, 1 Cyclotron Road, mail stop 2R0300, Berkeley CA  
94720-8198

Key Points:

Organic aerosol particle deformation is analyzed with x-ray microscopy

Amount of deformation is related to viscosity and surface tension of particles

Deformation of ambient and laboratory generated particles are compared

Index Terms

Atmospheric Composition and Structure: Aerosols and particles, instruments and techniques

Keywords

Aerosol, viscosity, STXM, microscopy

29 **Abstract**

30           The size and thickness of organic aerosol particles from five field campaigns were  
31 compared to those of laboratory generated secondary organic aerosols (SOA) using scanning  
32 transmission x-ray microscopy (STXM). Impacted organic particles were identified and the total  
33 carbon absorbance (TCA) was analyzed as a function of the area equivalent diameter of the  
34 particle on the substrate. Because they flatten less upon impaction, particles with higher  
35 viscosity and surface tension can be identified by a steeper slope on a plot of TCA vs. size. The  
36 slopes of the ambient data are statistically similar indicating a small range of average viscosities  
37 and surface tensions across five field campaigns. Steeper slopes were observed for the plots  
38 corresponding to ambient particles, while smaller slopes were indicative of the laboratory  
39 generated SOA. This suggests that, on average, ambient organic particles have higher viscosities  
40 and surface tensions than the more liquid like laboratory generated SOA particles.

41

42

43

44

45

46

47

48

## 49 **1. Introduction**

50           Organic aerosols constitute a significant fraction of atmospheric fine mode particulate  
51 matter [Zhang *et al.*, 2007]. Models of secondary organic aerosol (SOA) formation and aging  
52 assume that SOA consists of liquid particles with condensed phase diffusion rates that are fast  
53 enough to maintain equilibrium with the gas phase [Pankow, 1994; Hallquist *et al.*, 2009].  
54 However, recent studies examining particle bounce behavior [Virtanen *et al.*, 2010], response to  
55 physical manipulation [Renbaum-Wolff *et al.*, 2013], evaporation [Vaden *et al.*, 2011; Abramson  
56 *et al.*, 2013; Loza *et al.*, 2013], thermal desorption [Cappa and Wilson, 2011], particulate nitrate  
57 uptake [Perraud *et al.*, 2012], ammonia uptake [Kuwata and Martin, 2012], and diffusion  
58 [Vaden *et al.*, 2010] provide evidence that both laboratory and ambient particles can have higher  
59 viscosities. Most studies have been done on small sample sizes with little inter-comparison  
60 across ambient samples and only few studies [Virtanen *et al.*, 2010; Vaden *et al.*, 2011]  
61 compared laboratory and ambient samples. An investigation of the phase state or viscosity of  
62 particles from different geographical locations and under a range of conditions would provide an  
63 opportunity to examine existing assumptions about chemical composition and kinetics and to  
64 constrain the range of viscosity values appropriate for SOA models.

65           When an aerosol particle impacts a surface, some kinetic energy is dissipated in  
66 deformation. If the kinetic energy loss is large enough that the adhesion energy exceeds the  
67 rebound energy, the particle will remain on the surface. The elastic properties (viscosity), the  
68 surface properties (surface tension), and the liquid flow properties (whether the material is non-  
69 Newtonian or not) [Ivosevic *et al.*, 2006] determine both the adhesion probability and the final  
70 shape of the impacted particle. In this work, we compare the size and thickness of the impacted  
71 particles measured by scanning transmission X-ray microscopy/near-edge X-ray absorption fine

72 structure (STXM/NEXAFS) in order to probe particle deformation and provide useful  
73 information on particle properties.

74

## 75 **2. Experimental**

76 Ambient aerosols were collected over five field campaigns between 2001 and 2010.  
77 Figure 1 shows the geographic locations of these field sites. All of the campaigns were in North  
78 and South America. Two were in California: CARES (2010) in the Sacramento Valley [*Zaveri*  
79 *et al.*, 2012] and YACS (2002) in Yosemite National Park [*Hand et al.*, 2005]. The NAOPEX  
80 campaign (2001) [*Zaveri et al.*, 2010], MILAGRO campaign (2006) [*Moffet et al.*, 2010a], and  
81 VOCALS (2008) [*Wood et al.*, 2011] took place in the Boston area, the Mexico City  
82 metropolitan area, and in Chile respectively.

83 Laboratory samples were generated using a 5 m<sup>3</sup> Teflon chamber with UV-B broadband  
84 lamps in the absence of inorganic seed particles [*Nguyen et al.*, 2011a]. All chamber  
85 experiments were done in a dry chamber (relative humidity (RH) < 2%) that was flushed  
86 overnight with dried air between experiments. The isoprene samples had ~100 µl H<sub>2</sub>O<sub>2</sub> (Aldrich,  
87 30% by volume in water) injected into a glass bulb and evaporated into the chamber with dry air  
88 followed by a similar injection and evaporation of ~20 µl of isoprene (Aldrich, 99% purity). For  
89 the high NO<sub>x</sub> (HNO<sub>x</sub>) experiments, a small, controlled volume of gas from a NO cylinder  
90 (Praxair, 5000 ppm NO in N<sub>2</sub>) was injected in the chamber. The starting mixing ratios of  
91 isoprene and H<sub>2</sub>O<sub>2</sub> were 1 ppm and 6 ppm, respectively. For the HNO<sub>x</sub> experiment, the initial  
92 mixing ratios of NO and NO<sub>y</sub> were ~400 and 500 ppb, respectively; the NO<sub>x</sub> level was below the  
93 detection limit (2 ppb) in the low-NO<sub>x</sub> (LNO<sub>x</sub>) experiments. Photooxidation times were 2-3  
94 hours. Limonene SOA was generated by injecting *d*-limonene (10 µl → 300 ppb) and ozone

95 (~600 ppb) into the dry, dark chamber. Additional samples were prepared using a flow tube  
96 [*Bones et al.*, 2010]. Either *d*-limonene or  $\alpha$ -pinene was introduced into a flow of zero air (H<sub>2</sub>O,  
97 CO<sub>2</sub>, and VOC's removed) and dry ozone using a syringe pump at liquid flow rates of 16 and 25  
98  $\mu$ l/hr, respectively. Additional information on particle generation and instrumentation is  
99 provided in the auxiliary material.

100 Ambient samples were collected using a TRAC (time-resolved aerosol collector) sampler  
101 with an effective cutoff size,  $d_{50}$ , of 0.36-0.38  $\mu$ m [*Laskin et al.*, 2006]. Copper-grid-supported  
102 carbon B films and silicon nitride (Si<sub>3</sub>N<sub>4</sub>) coated Si frames were used as impaction substrates.  
103 Minimal differences in impaction behavior and, since both substrates are hydrophobic, minimal  
104 differences in the effect on surface tension are expected between the two substrates. Laboratory  
105 samples were collected on the seventh and eighth stages of a rotating MOUDI (multi-orifice  
106 uniform-deposit impactor, MSP 110-R) with aerodynamic cut points of 0.32  $\mu$ m and 0.18  $\mu$ m,  
107 respectively [*Marple et al.*, 1991] using Si<sub>3</sub>N<sub>4</sub> coated Si frames as substrates. The impactor RH  
108 is equal to the ambient RH times the ratio of the impactor pressure to the ambient pressure  
109 [*Saukko et al.*, 2012]. Since the absolute pressure at the exit of the MOUDI's sixth and seventh  
110 stages is 95-97% of the inlet pressure, the particles experience negligible changes in RH during  
111 impaction. For the TRAC, the pressure in the sampling area is reduced to 70% of the ambient  
112 pressure, but, the  $\sim$ 30  $\mu$ s spent in the impaction region (between the nozzle and the impaction  
113 surface) is insufficient for equilibration of the  $\sim$ 300-400 nm aerodynamic diameter particles with  
114 respect to the water uptake/loss prior to impaction [*Koop et al.*, 2011; *Saukko et al.*, 2012].  
115 However, since the samples remain in the reduced pressure region, after impaction, for the  
116 duration of the sampling time, loss of higher volatility compounds is likely. The amount of loss  
117 may be sample dependent, and this is a potential source for some of the scatter in the data.

118           The final particle shape is related to the impaction velocity/kinetic energy, the viscosity  
119 and surface tension, and the fluid flow properties [*Ivosevic et al.*, 2006]. In the TRAC sampler,  
120 the particle impaction velocity is ~90 m/s, while in the MOUDI, on stage 7, the velocity is ~36  
121 m/s [*Marple et al.*, 1991; *Laskin et al.*, 2006]. Therefore, any comparison between samples  
122 collected with these two techniques must take into account that, due to the difference in  
123 impaction velocities, identical particles collected with the TRAC will deform more than similar  
124 particles collected with the MOUDI.

125           The scanning transmission X-ray microscopy/near-edge X-ray absorption fine structure  
126 (STXM/NEXAFS) measurements were taken at the Advanced Light Source at Lawrence  
127 Berkeley National Laboratory on beamlines 11.0.2 and 5.3.2.2. The operation of the microscope  
128 has been explained in detail by Kilcoyne et al. [2003]. Briefly, samples were held at the focal  
129 point (30-40 nm spot size) and raster scanned. Transmitted X-rays were detected, the X-ray  
130 photon energy was incremented, and images at four energies (278, 285.4, 288, and 320 eV) were  
131 collected. The work presented here uses analysis of images collected at the carbon K-edge,  
132 focusing on 278 and 320 eV. These energies correspond to absorbance due to the carbon pre-  
133 edge and post-edge, respectively [*Moffet et al.*, 2010b]. The STXM measurements were  
134 performed under vacuum; an initial pump down to ~100 mTorr and then backfilled with He to 20  
135 Torr.

136           STXM/NEXAFS data were imported into MatLab software for further analysis [*Moffet et*  
137 *al.*, 2010b]. The pixels determined to contain particles were assigned an intensity value ( $I$ ), the  
138 particle-free pixels were assigned a background intensity value ( $I_0$ ), and the absorbance or optical  
139 density (OD) was calculated via the equation:

140

141 
$$\text{OD} = -\ln(I/I_0) = \mu\rho d$$
 Equation 1

142

143 where  $\mu$  is the mass absorption coefficient ( $\text{cm}^2/\text{g}$ ),  $\rho$  is the density ( $\text{g}/\text{cm}^3$ ), and  $d$  is the  
144 thickness of the particle (cm). By examining the difference in optical density between the post-  
145 edge and the pre-edge, the thickness of the carbon or the total carbon absorbance (TCA) can be  
146 calculated (subscripts correspond to the X-ray photon energies) [Moffet *et al.*, 2011].

147

148 
$$\text{TCA} = \text{OD}_{320} - \text{OD}_{278}$$
 Equation 2

149

150 Three component types were identified by the MatLab script: organic, inorganic, and elemental  
151 carbon or soot [Moffet *et al.*, 2010b]. Only particles identified as predominantly organic, without  
152 any inorganic dominant regions or soot inclusions, were selected for the data sets presented in  
153 this manuscript. Some particles and particle components were non-spherical; hence, the sizes are  
154 reported as area equivalent diameters (AED). The auxiliary material contains additional  
155 information on the data collection and analysis.

156

### 157 **3. Results and Discussion**

158 Figure 2 displays the best fit lines for the size of impacted particles vs. the TCA for all  
159 data sets. The data for the ambient particles are shown with solid lines and dashed lines are used  
160 for the laboratory particles. A steeper slope indicates that the particles have flattened less during  
161 impaction, and thus, have a higher viscosity and/or surface tension. Plots of full data sets and  
162 corresponding fitting parameters are provided in Figures S1-S2 and Tables S1-S2. The red and  
163 blue shaded areas highlight the range of the  $\pm 95\%$  confidence intervals for the ambient and



164 laboratory particles respectively. The slope of each ambient data set falls within the 95%  
165 confidence intervals of the other data sets consistent with similar viscosities and/or surface  
166 tensions between the samples. This similarity indicates that a small range of viscosity and/or  
167 surface tension values may adequately describe the average aerosol population used in SOA  
168 models.

169 In Figure 2 all of the laboratory samples have smaller slopes than ambient samples. Four  
170 of the laboratory samples' slopes lie within the 95% confidence intervals of the each other.  
171 Thus, the different oxidants, precursors, and different conditions (chamber vs. flow tube)  
172 sampled here have minimal effect on the viscosities and/or surface tensions of the aerosols  
173 formed. The isoprene sample generated under HNO<sub>x</sub> conditions is the outlier, outside the 95%  
174 confidence intervals of the other samples, with a slightly negative slope. The negative slope  
175 arises because the slope of OD<sub>320</sub> vs. size (Table S3) is nearly zero and the OD<sub>278</sub> is slightly  
176 higher, but within the 95% confidence interval, than the OD<sub>320</sub>. Pre-edge absorbance (OD<sub>278</sub>)  
177 arises from absorption and a small contribution from scattering of other atoms such as nitrogen,  
178 oxygen, sulfur, etc. Post-edge absorbance (OD<sub>320</sub>) is due to absorption and scattering from  
179 carbon as well as the other atoms. Photooxidation of isoprene under HNO<sub>x</sub> conditions is known  
180 to generate compounds with higher O/C ratio and significant nitrogen content compared to the  
181 LNO<sub>x</sub> conditions [Nguyen *et al.*, 2011b]. However, since the slope of the OD<sub>320</sub> vs. size is  
182 outside the 95% confidence intervals of the other laboratory samples (Table S3) the scattering  
183 and absorption by the heteroatoms does fully account for the smaller slope for the HNO<sub>x</sub> sample,  
184 which means the particles have a lower viscosity/surface tension. Potential reasons for these  
185 differences include (1) isoprene particles formed under HNO<sub>x</sub> conditions and under LNO<sub>x</sub>  
186 conditions have different chemical compositions [Nguyen *et al.*, 2011b] and (2) the HNO<sub>x</sub>

187 aerosols formed more quickly and were in the chamber for a shorter period of time (~2 hrs. for  
188 HNO<sub>x</sub> vs. ~3 hrs. for the LNO<sub>x</sub> experiments).

189         The difference between ambient and laboratory aerosol particles is consistent with  
190 observations of slower evaporation kinetics for ambient SOA compared to laboratory generated  
191 SOA [*Vaden et al.*, 2011]. However, Virtanen et al. [2010] reported a higher bounce fraction for  
192 chamber SOA than that for atmospheric SOA which is consistent with higher viscosity/more  
193 glassy particles in their chamber compared to the ambient. It is important to note that their  
194 chamber SOA was generated from a mixture of all of the volatile organic compounds (VOCs)  
195 emitted by pine seedlings. Thus, a difference between our results and the results of Virtanen  
196 could be that our laboratory experiments used a single VOC precursor rather than a complex  
197 mixture.

198         A variety of techniques have indicated that laboratory generated particles are amorphous  
199 semi-solid particles [*Vaden et al.*, 2010; *Virtanen et al.*, 2010; *Cappa and Wilson*, 2011; *Vaden et*  
200 *al.*, 2011; *Kuwata and Martin*, 2012; *Perraud et al.*, 2012]. In contrast, the data from this study  
201 show that the laboratory generated particles have smaller slopes than the ambient particles. The  
202 analysis presented here examines deformation behavior of particles upon impactation. Since  
203 deformation depends upon both viscosity and surface tension, a direct comparison between the  
204 relative deformation behaviors observed here and the viscosities reported in other studies should  
205 be made with caution. However, the laboratory conditions used here are fairly typical, and thus,  
206 the results showing lower viscosity/surface tension for laboratory particles compared to ambient  
207 particles are relevant for a wide range of laboratory studies.

208         Figure 3 shows the particle size as a function of the optical density at the pre-edge,  
209 OD<sub>278</sub>. The black data points are the combined ambient data and the red data points are the

210 combined laboratory generated data. The slope of the best fit line for the ambient data is an  
211 order of magnitude higher than the slope for the laboratory generated particles. The pre-edge  
212 absorbance is due to absorbance and scattering by atoms other than carbon such as O, N, S, etc.  
213 and the difference in slopes indicate that the ambient particles have more heteroatoms than the  
214 laboratory generated particles. Most likely, there are significantly more organo-sulfates and  
215 organo-nitrates in the ambient particles, or there are small amounts of inorganic species such as  
216  $(\text{NH}_4)_2\text{SO}_4$ , that do not crystalize into a large inclusion and are instead finely dispersed through  
217 the particle. The contribution from other absorbing and scattering elements was estimated by  
218 calculating the thickness ratio of organic to inorganic components using  $\text{OD}_{278}$  and  $\text{OD}_{320}$   
219 measurements and estimates of the mass absorption coefficients and densities for both organic  
220 and inorganic species (for calculations see Auxiliary material). Approximately 11-30% of the  
221 thickness for the particles is likely due to non-organic molecules or atoms. The most likely  
222 species are  $(\text{NH}_4)_2\text{SO}_4$  and NaCl, but nano-particles that contain other elements commonly  
223 observed in atmospheric aerosols [Moffet *et al.*, 2010a] are also possible.

224         There are numerous possible reasons for the observed differences between laboratory  
225 generated and ambient aerosols. Aerosols in smog chambers are more concentrated prompting  
226 smaller, semi-volatile organic compounds (SVOC), which would normally exist in gaseous  
227 phase under typical ambient conditions, to partition in particles, potentially making the particles  
228 more liquid like. The semi-volatile compounds may be lost during measurements since STXM is  
229 performed under vacuum and the potentially larger amount of SVOC in the chamber experiments  
230 could make the particles more optically thin. Chamber particles have reacted for a shorter length  
231 of time than aerosols in the ambient environment [Ng *et al.*, 2010]. In the chamber experiments  
232 only a single precursor was used, whereas ambient samples can have a wide range of precursors.

233 Finally, no inorganic compounds were used in the chamber studies which may impact the  
234 chemical composition of the particles and ultimately the particle phase state. Our results  
235 demonstrate that the chemical compositions and potentially the reaction kinetics of laboratory  
236 aerosols differ significantly from those in the ambient environment.

237

#### 238 **4. Summary and Conclusions**

239 We investigated the amount of deformation of impacted aerosol particles from both  
240 ambient field campaigns and laboratory studies using STXM/NEXAFS analysis of the TCA and  
241 the size of the particles. Samples with steeper slopes on a plot of TCA vs. size have higher  
242 viscosities/surface tensions. The slopes for the ambient samples all fell within the 95%  
243 confidence interval of each other. The laboratory generated samples all had lower slopes than the  
244 ambient samples indicating lower viscosities/surface tensions than for particles measured during  
245 ambient field campaigns. The differences in aging time, aerosol mass concentration, volatility,  
246 number of precursors, and lack of any inorganic compounds in the laboratory samples likely  
247 contribute to these results. The lower viscosities/surface tensions in the laboratory samples  
248 impacts the kinetics of SOA formation, gas-particle partitioning, and chemical composition of  
249 the laboratory generated aerosols as compared to ambient aerosols. Thus, caution should be used  
250 when comparing the results of laboratory experiments to ambient samples and when applying  
251 data from laboratory studies to SOA models. The results of this study indicate that a small range  
252 of viscosities/surface tensions may be appropriate to describe the average ambient aerosol  
253 population in SOA models.

254

255

256 **Acknowledgements**

257 Data supporting Figure 2 and Figure 3 are available in the Supporting information, Table S6.

258 This work was supported in part by the U.S. Department of Energy's Atmospheric System  
259 Research, an Office of Science, Office of Biological and Environmental Research program.

260 STXM/NEXAFS was done at beamlines 5.3.2.2 and 11.0.2 at The Advanced Light Source at  
261 Lawrence Berkeley National Laboratory (LBNL).which are supported by the Director, Office of  
262 Science, Office of Basic Energy Sciences, (beamline 11.0.2 is also supported by the Division of  
263 Chemical Sciences, Geosciences, and Biosciences) of the U.S. Department of Energy under  
264 Contract No. DE-AC02-05CH11231. The UCI team acknowledges support from the National  
265 Science Foundation Grant CHE-0909227.

2661.

267 **Disclaimers.** Publications must include the following disclaimer:

268a. This document was prepared as an account of work sponsored by the United States Government.  
269 While this document is believed to contain correct information, neither the United States Government  
270 nor any agency thereof, nor the Regents of the University of California, nor any of their employees,  
271 makes any warranty, express or implied, or assumes any legal responsibility for the accuracy,  
272 completeness, or usefulness of any information, apparatus, product, or process disclosed, or  
273 represents that its use would not infringe privately owned rights. Reference herein to any specific  
274 commercial product, process, or service by its trade name, trademark, manufacturer, or otherwise,  
275 does not necessarily constitute or imply its endorsement, recommendation, or favoring by the United  
276 States Government or any agency thereof, or the Regents of the University of California. The views  
277 and opinions of authors expressed herein do not necessarily state or reflect those of the United  
278 States Government or any agency thereof or the Regents of the University of California.

2792. **Copyright notice.** Publication submissions must include the following copyright notice:

280a. This manuscript has been authored by an author at Lawrence Berkeley National Laboratory under  
281 Contract No. DE-AC02-05CH11231 with the U.S. Department of Energy. The U.S. Government  
282 retains, and the publisher, by accepting the article for publication, acknowledges, that the U.S.  
283 Government retains a non-exclusive, paid-up, irrevocable, world-wide license to publish or reproduce  
284 the published form of this manuscript, or allow others to do so, for U.S. Government purposes.  
285

286

287

288

289

290

291

292

293

294

295

296

297

298

## 299 **References**

- 300 Abramson, E., et al. (2013), Experimental determination of chemical diffusion within secondary  
301 organic aerosol particles, *Physical Chemistry Chemical Physics* 15(8): 2983-2991.  
302 Bones, D. L., et al. (2010), Appearance of strong absorbers and fluorophores in limonene-O<sub>3</sub>  
303 secondary organic aerosol due to NH<sub>4</sub><sup>+</sup>-mediated chemical aging over long time scales,  
304 *Journal of Geophysical Research-Atmospheres*, 115, D05203, doi:10.1029/2009JD012864.  
305 Cappa, C. D. and K. R. Wilson (2011), Evolution of organic aerosol mass spectra upon heating:  
306 implications for OA phase and partitioning behavior, *Atmospheric Chemistry and Physics*  
307 11(5): 1895-1911.  
308 Hallquist, M., et al. (2009), The formation, properties and impact of secondary organic aerosol:  
309 current and emerging issues, *Atmospheric Chemistry and Physics* 9(14): 5155-5236.

310 Hand, J. L., et al. (2005), Optical, physical, and chemical properties of tar balls observed during  
311 the Yosemite Aerosol Characterization Study. *Journal of Geophysical Research-*  
312 *Atmospheres* 110, D21210, doi:10.1029/2004JD005728.

313 Ivošević, M., et al. (2006), 3D predictions of thermally sprayed polymer splats: Modeling  
314 particle acceleration, heating and deformation on impact with a flat substrate, *International*  
315 *Journal of Heat and Mass Transfer* 49(19-20): 3285-3297.

316 Kilcoyne, A. L. D., et al. (2003), Interferometer-controlled scanning transmission X-ray  
317 microscopes at the Advanced Light Source, *Journal of Synchrotron Radiation* 10: 125-136.

318 Koop, T., et al. (2011), Glass transition and phase state of organic compounds: dependency on  
319 molecular properties and implications for secondary organic aerosols in the atmosphere,  
320 *Physical Chemistry Chemical Physics* 13(43): 19238-19255.

321 Kuwata, M. and S. T. Martin (2012), Phase of atmospheric secondary organic material affects its  
322 reactivity, *Proceedings of the National Academy of Sciences of the United States of America*  
323 109(43): 17354-17359.

324 Laskin, A., et al. (2006), Analysis of individual environmental particles using modern methods  
325 of electron microscopy and X-ray microanalysis, *J. Electron Spectrosc. Relat. Phenom.*  
326 150(2-3): 260-274.

327 Loza, C. L., et al. (2013), On the Mixing and Evaporation of Secondary Organic Aerosol  
328 Components, *Environmental Science & Technology* 47(12): 6173-6180.

329 Marple, V. A., et al. (1991), A Microorifice Uniform Deposit Impactor (MOUDI)  
330 - Description, Calibration, And Use, *Aerosol Science and Technology* 14(4): 434-446.

331 Moffet, R. C., et al. (2010a), Microscopic characterization of carbonaceous aerosol particle aging  
332 in the outflow from Mexico City, *Atmospheric Chemistry and Physics* 10(3): 961-976.

333 Moffet, R. C., et al. (2010b), Automated Chemical Analysis of Internally Mixed Aerosol  
334 Particles Using X-ray Spectromicroscopy at the Carbon K-Edge, *Anal Chem* 82(19): 7906-  
335 7914.

336 Moffet, R. C., et al. (2011). Scanning Transmission X-ray Microscopy Applications in  
337 Atmospheric Aerosol Research, *Fundamentals and Applications in Aerosol Spectroscopy*. R.  
338 Signorell and J. P. Reid. Boca Raton, FL, CRC Press, Taylor & Francis Group: 434-436.

339 Ng, N. L., et al. (2010), Organic aerosol components observed in Northern Hemispheric datasets  
340 from Aerosol Mass Spectrometry, *Atmospheric Chemistry and Physics* 10(10): 4625-4641.

341 Nguyen, T. B., et al. (2011a), Effect of humidity on the composition of isoprene photooxidation  
342 secondary organic aerosol, *Atmospheric Chemistry and Physics* 11(14): 6931-6944.

343

344 Nguyen, T. B., et al. (2011b), Nitrogen-Containing Organic Compounds and Oligomers in  
345 Secondary Organic Aerosol Formed by Photooxidation of Isoprene, *Environmental Science*  
346 *& Technology* 45(16): 6908-6918.

347 Pankow, J. F. (1994), An Absorption-Model of Gas-Particle Partitioning of  
348 Organic-Compounds In The Atmosphere, *Atmospheric Environment* 28(2): 185-188.

349 Perraud, V., et al. (2012), Nonequilibrium atmospheric secondary organic aerosol formation and  
350 Growth, *Proceedings of the National Academy of Sciences of the United States of America*  
351 109(8): 2836-2841.

352 Renbaum-Wolff, L., et al. (2013), Viscosity of alpha-pinene secondary organic material and  
353 implications for particle growth and reactivity, *Proceedings of the National Academy of*  
354 *Sciences of the United States of America* 110(20): 8014-8019.

355 Saukko, E., et al. (2012), A method to resolve the phase state of aerosol particles, *Atmospheric*

356 *Measurement Techniques* 5(1): 259-265.

357 Vaden, T. D., et al. (2010), Morphology of mixed primary and secondary organic particles and  
 358 the adsorption of spectator organic gases during aerosol formation, *Proceedings of the*  
 359 *National Academy of Sciences of the United States of America* 107(15): 6658-6663.

360 Vaden, T. D., et al. (2011), Evaporation kinetics and phase of laboratory and ambient secondary  
 361 organic aerosol, *Proceedings of the National Academy of Sciences of the United States of*  
 362 *America* 108(6): 2190-2195.

363 Virtanen, A., et al. (2010), An amorphous solid state of biogenic secondary organic aerosol  
 364 Particles, *Nature* 467(7317): 824-827.

365 Wood, R., et al. (2011), The VAMOS Ocean-Cloud-Atmosphere-Land Study Regional  
 366 Experiment (VOCALS-REx): goals, platforms, and field operations, *Atmospheric Chemistry*  
 367 *and Physics* 11(2): 627-654.

368 Zaveri, R. A., et al. (2010), Nighttime chemical evolution of aerosol and trace gases in a power  
 369 plant plume: Implications for secondary organic nitrate and organosulfate aerosol formation,  
 370 NO<sub>3</sub> radical chemistry, and N<sub>2</sub>O<sub>5</sub> heterogeneous hydrolysis, *Journal of Geophysical*  
 371 *Research-Atmospheres* 115, D12304, doi:10.1029/2009JD013250.

372 Zaveri, R. A., et al. (2012), Overview of the 2010 Carbonaceous Aerosols and Radiative Effects  
 373 Study (CARES), *Atmospheric Chemistry and Physics* 12(16): 7647-7687.

374 Zhang, Q., et al. (2007), Ubiquity and dominance of oxygenated species in organic aerosols in  
 375 anthropogenically-influenced Northern Hemisphere midlatitudes, *Geophysical Research*  
 376 *Letters* 34(13), L13801, doi:10.1029/2007GL029979.

377  
378  
379  
380  
381  
382  
383  
384

385 **Table 1.** Ambient and laboratory fitting results for TCA vs. size<sup>a</sup>

Campaign	Slope	Intercept	Sample	Slope	Intercept
CARES	0.090±0.004	0.0079±0.002	Isoprene-LNOx	0.031±0.006	0.025±0.003
MILAGRO	0.077±0.01	0.029±0.005	Isoprene-HNOx	-0.011±0.01	0.023±0.005
NAOPEX	0.084±0.01	0.020±0.01	α-pinene-flow tube	0.036±0.008	0.048±0.009



VOCALS	0.10±0.03	0.018±0.01	Limonene-flow tube	0.039±0.009	0.023±0.005
YACS	0.11±0.03	0.0043±0.01	Limonene-chamber	0.042±0.006	0.028±0.005

386 <sup>a</sup>The ±95% confidence intervals for the slope and intercept are given.

387

388

389

390

391

392

393

394

395

396

397

398

399

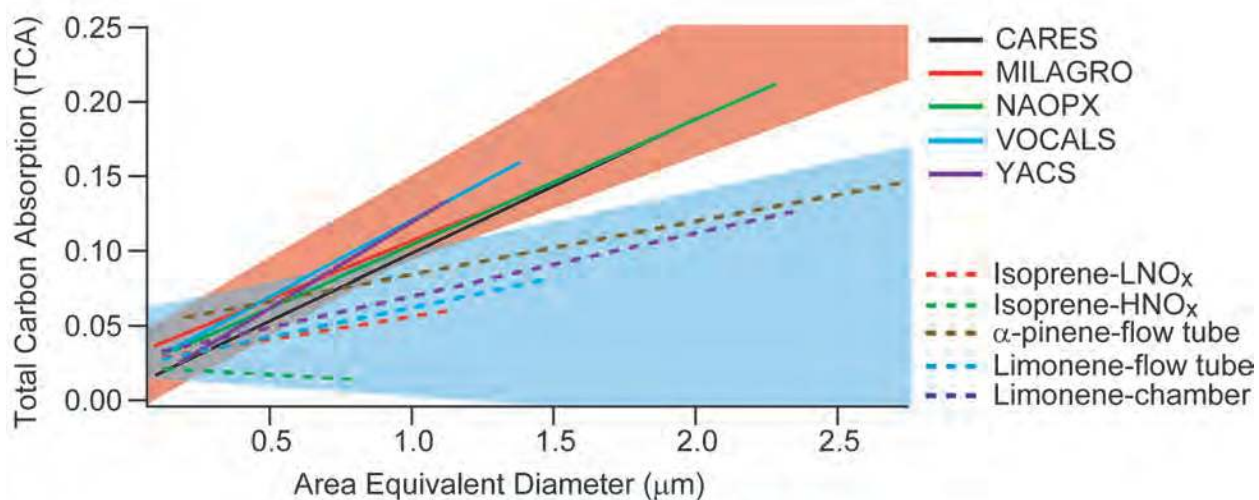
400

401

402 **Figures**



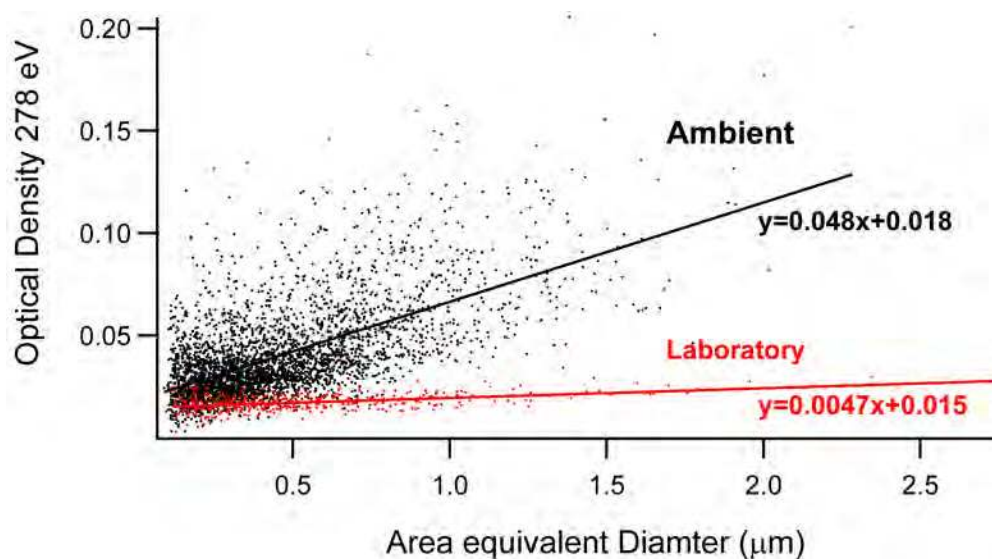
403  
 404 **Figure 1.** Map showing the geographic locations of the five field campaigns. Samples from the  
 405 VOCALS campaign in Chile and the NAOPEX campaign in the Boston area were aerial  
 406 samples, MIAGRO, CARES, and YACS samples were collected at the ground sites.  
 407



408  
 409 **Figure 2.** Optical thickness of carbon (total carbon absorption) as a function of size of the

410 impacted organic particles. Solid lines: best fit lines for the ambient particles, dashed lines: best  
411 fit lines for the laboratory generated particles. The red and blue triangles highlight the range of  
412 the  $\pm 95\%$  confidence intervals for the ambient and laboratory samples respectively. LNO<sub>x</sub> and  
413 HNO<sub>x</sub> refer to low-NO<sub>x</sub> and high-NO<sub>x</sub> oxidation by OH; ozone is used as the oxidant for the  
414 remaining samples.

415  
416  
417  
418  
419  
420  
421  
422  
423



424

425 **Figure 3.** Optical density at 278 eV (pre-edge) vs. size (area equivalent diameter). Black: all  
426 ambient samples, red: all laboratory samples. The best fit lines and equations are shown for each  
427 data set. The data are consistent with a higher fraction of non-carbon elements in the ambient  
428 samples.

1 **Draft 5**

2 **Phase State and Physical Properties of Ambient and Laboratory**  
3 **Generated Secondary Organic Aerosol**

4  
5 **Rachel E. O'Brien,<sup>1,2\*</sup> Alexander Neu,<sup>1</sup> Scott A. Epstein,<sup>3</sup> Amanda C. MacMillan,<sup>3</sup> Sergey**  
6 **A. Nizkorodov,<sup>3</sup> Alexander Laskin,<sup>4</sup> Ryan C. Moffet,<sup>2</sup> Mary K. Gilles,<sup>1</sup>**

7 [1] Chemical Sciences Division, Lawrence Berkeley National Laboratory, Berkeley, California,  
8 94720-8198, USA

9 [2] Department of Chemistry, University of the Pacific, Stockton, CA 95211, USA

10 [3] Department of Chemistry, University of California, Irvine, CA 92697-2025, USA

11 [4] William R. Wiley Environmental and Molecular Sciences Laboratory, Pacific Northwest  
12 National Laboratory, Richland, WA, 99352, USA

13  
14 \*Address correspondence to the following author

15 Email: resellon@lbl.gov

25

## 26 **Supplemental Information**

27

### 28 **Laboratory generated samples**

29 Experimental conditions for chamber experiments are given in Table S4 (the tables and  
30 figures are numbered in the order of appearance in the main manuscript). For the flow tube  
31 experiments, the flow tube was operated at low RH (< 2%), ambient temperature (~25 °C), with  
32 the lights turned off. The oxidant was ozone (30-50 ppm) produced by flowing oxygen gas  
33 through a commercial ozone generator. The flow tube residence time was ~5 min. In both cases  
34 (chamber and flow tube) samples were collected on stages 7 and 8 of a 10 stage rotating cascade  
35 impactor (MOUDI 110-R, MSP) using Si<sub>3</sub>N<sub>4</sub> windows taped to aluminum substrates. Collection  
36 times were ~30-45 min for chamber experiments and ~1 min for flow tube experiments.

37

38

### 39 **Data Collection/Analysis**

40 Because of the poor signal to noise ratio, particles with average OD<sub>320</sub> values < 0.03 were  
41 excluded from analysis. For I<sub>0</sub> values of ~ 7,000 counts/ms, this cutoff corresponds to about 200  
42 photons/ms. Since stray light in the STXM leads to approximately 100-200 photons/ms noise,  
43 the particles with the lowest average OD have the largest relative amount of noise.

44 Since some particles and particle components were non-spherical, the sizes reported are  
45 the area equivalent diameters (AED), defined as a diameter of a hemisphere required to cover the  
46 same area as the projection of the particles on the surface:

$$47 \quad \text{AED} = 2\sqrt{\left(\frac{\text{length}_x \times \text{length}_y}{\pi}\right)} \quad \text{Equation S1}$$

48 where  $length_x$  and  $length_y$  are the effective sizes of the particle in the x and y dimensions.

49

## 50 **Absorption Coefficients**

51 Organic material mass absorption coefficients  $\mu$  ( $\text{cm}^2/\text{g}$ ) were obtained from the sum of  
52 the absorption cross sections of the constituent atoms by:

53

$$54 \quad \mu = \frac{N_A}{MW} \sum_i x_i \sigma_{ai} \quad \text{Equation S2}$$

55

56 where  $MW$  is the molecular weight of the compound containing  $x_i$  atoms of type  $i$ ,  $\sigma_a$  is the total  
57 atomic absorption cross section ( $\text{cm}^2/\text{atom}$ ) for this type of atom, and  $N_A$  is the Avogadro's  
58 number. This approximation neglects interactions between the atoms in the material and is  
59 applicable at photon energies sufficiently far from absorption edges [*Henke et al.*, 1993;  
60 *Thomson et al.*, 2009]. Using the list of chemical formulas from negative mode high resolution  
61 mass spectrometry analysis of ambient particles (O'Brien et al., manuscript in preparation,  
62 2014), the mass absorption coefficient was calculated and plotted as a function of the O/C value  
63 (Figure S3). An estimate for the average O/C value of 0.44 [*Setyan et al.*, 2012] leads to  $\mu_{320} \cong$   
64  $22,500 \text{ cm}^2/\text{g}$  and  $\mu_{278} \cong 1102 \text{ cm}^2/\text{g}$ .

65

## 66 **Inorganic Contributions**

67 The particles used in this analysis were identified as organic using the MatLab script  
68 [*Moffet et al.*, 2010b]. However, aerosol particles that are primarily organic can also have  
69 inorganic components. To estimate the fraction of other elements in these particles we examined

70 the OD at the carbon pre-edge (278 eV) and the post edge (320 eV) of a particle with inorganic  
71 and organic components via equations S3 and S4:

72

$$73 \quad OD_{278} = \mu_{org,278}\rho_{org}d_{org} + \mu_{in,278}\rho_{in}d_{in} \quad \text{Equation S3}$$

$$74 \quad OD_{320} = \mu_{org,320}\rho_{org}d_{org} + \mu_{in,320}\rho_{in}d_{in} \quad \text{Equation S4}$$

75

76 Where  $\mu_{org}, \rho_{org}$  is the linear absorption coefficient of the organic species,  $\mu_{in}, \rho_{in}$  is the linear  
77 absorption coefficient for the inorganic species, and  $d_{in}$  and  $d_{org}$  are the average sample  
78 thicknesses of the inorganic and organic, respectively. The thickness ratio [Moffet *et al.*, 2010b]  
79 can then be calculated by combining equations S3 and S4:

80

$$81 \quad \frac{d_{org}}{d_{in}} = \frac{OD_{320}\mu_{in,278}\rho_{in} - OD_{278}\mu_{in,320}\rho_{in}}{OD_{278}\mu_{org,320}\rho_{org} - OD_{320}\mu_{org,278}\rho_{org}} \quad \text{Equation S5}$$

82

83 To calculate the linear absorption coefficients for the organic terms, the  $\mu_{320}$  and  $\mu_{278}$  estimates  
84 from above and a density of 1.3 g/cm<sup>3</sup> [Setyan *et al.*, 2012] were used. For the inorganic terms,  
85 three cases were considered. In the first case, the linear absorption coefficients were calculated  
86 for elements with atomic numbers between 6 (carbon) and 26 (Iron) that have been observed in  
87 atmospheric aerosols [Moffet *et al.*, 2010a]. Elements with higher linear absorption coefficients  
88 will absorb more photons and at 278 eV Al, Si, P, S, Cr, Mg, and Fe all have higher linear  
89 absorption coefficients in the range of 7-13  $\mu\text{m}^{-1}$  (Figure S4a). At 320 eV the elements Si, P, S,  
90 Cl, Cr, Mn, and Fe all have coefficients between 5.6-10  $\mu\text{m}^{-1}$  (Figure S4b). Given these ranges,  
91 values of 10  $\mu\text{m}^{-1}$  at 278 eV and 8  $\mu\text{m}^{-1}$  at 320 eV were used. In the second case, the linear  
92 absorption coefficients for NaCl were used (8.1  $\mu\text{m}^{-1}$  at 278 eV and 6.3  $\mu\text{m}^{-1}$  at 320 eV). In the



93 last case, values for ammonium sulfate were used ( $3.2 \mu\text{m}^{-1}$  at 278 eV and  $2.4 \mu\text{m}^{-1}$  at 320 eV).  
94 Using these estimates and the measured  $\text{OD}_{278}$  and  $\text{OD}_{320}$  values, the average thickness ratio for  
95 each data set was calculated and is shown in Table S6. All of the data sets, with the exception of  
96 VOCALS, range from ~11-30% inorganic with higher percentages when all of the inorganic is  
97 assumed to be ammonium sulfate as the inorganic. The VOCALS data set has averages from  
98 ~22-47% indicating that the organic dominated particles in this campaign contain a larger  
99 contribution of inorganic species than the other campaigns. The particles from the VOCALS  
100 campaign were collected downwind of copper smelting plants with large sulfur emissions [Wood  
101 *et al.*, 2011]. Thus, for these campaigns, approximately 11-30% of the thickness for the organic  
102 particles is likely due to the absorption cross section contribution from non-organic molecules or  
103 atoms.

104

## 105 **References**

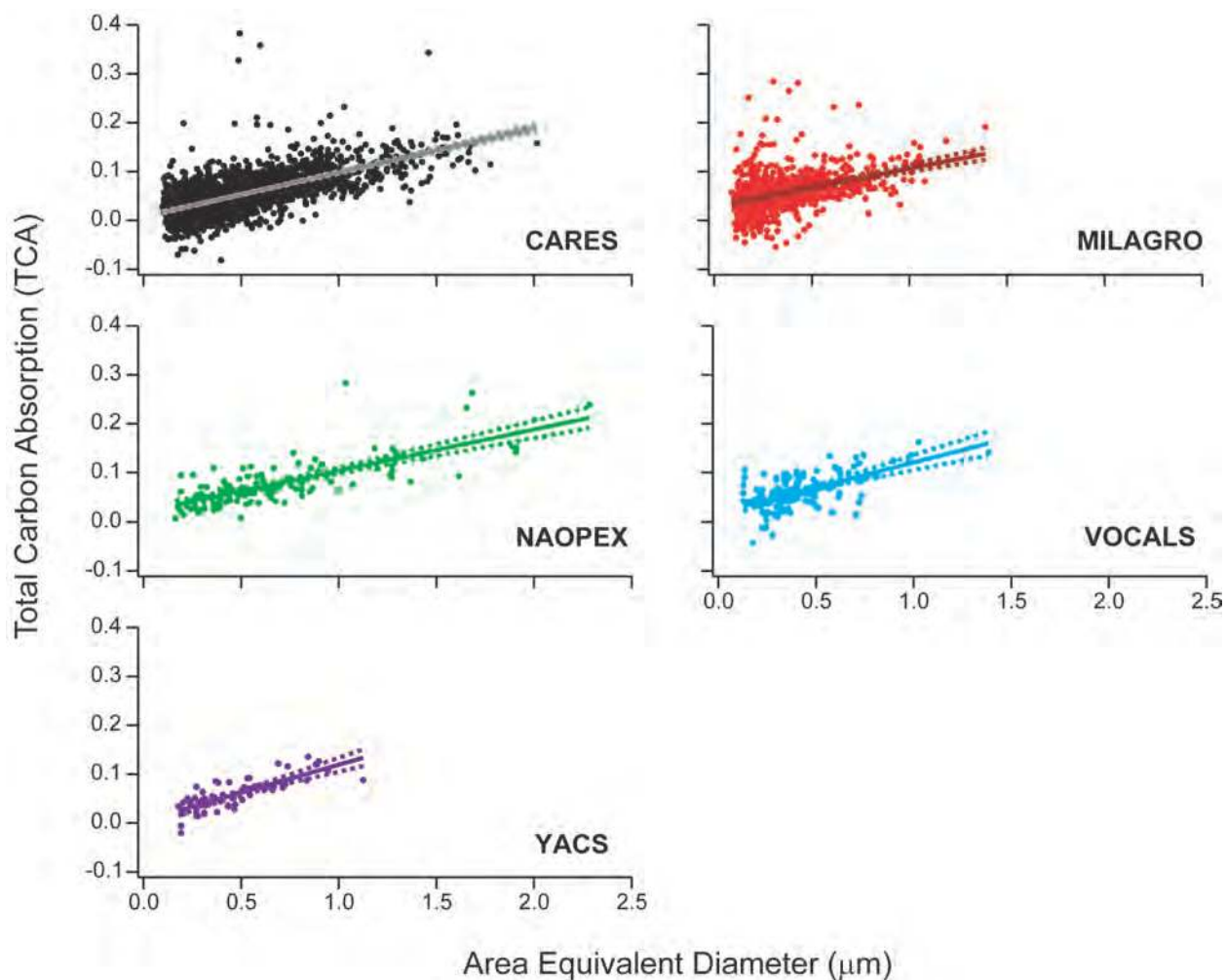
- 106 Henke, B. L., et al. (1993), X-Ray Interactions - Photoabsorption, Scattering, Transmission And  
107 Reflection at  $E=50\text{-}30,000$  EV,  $Z=1\text{-}92$  (VOL 54, PG 181, 1993). *Atom. Data Nucl. Data*  
108 *Tables 55(2)*: 349-349.
- 109 Moffet, R. C., et al. (2010a), Microscopic characterization of carbonaceous aerosol particle aging  
110 in the outflow from Mexico City, *Atmospheric Chemistry and Physics 10(3)*: 961-976.
- 111 Moffet, R. C., et al. (2010b), Automated Chemical Analysis of Internally Mixed Aerosol  
112 Particles Using X-ray Spectromicroscopy at the Carbon K-Edge, *Anal Chem 82(19)*: 7906-  
113 7914.
- 114 Setyan, A., et al. (2012), Characterization of submicron particles influenced by mixed biogenic  
115 and anthropogenic emissions using high-resolution aerosol mass spectrometry: results from  
116 CARES, *Atmospheric Chemistry and Physics 12(17)*: 8131-8156.
- 117 Thomson, A., et al. (2009). *Center for X-Ray Optics and Advanced Light Source X-Ray Data*  
118 *Booklet*. Lawrence Berkeley National Laboratory, Lawrence Berkeley National Laboratory.
- 119 Wood, R., et al. (2011), The VAMOS Ocean-Cloud-Atmosphere-Land Study Regional  
120 Experiment (VOCALS-REx): goals, platforms, and field operations, *Atmospheric Chemistry*  
121 *and Physics 11(2)*: 627-654.

122

123

124

125



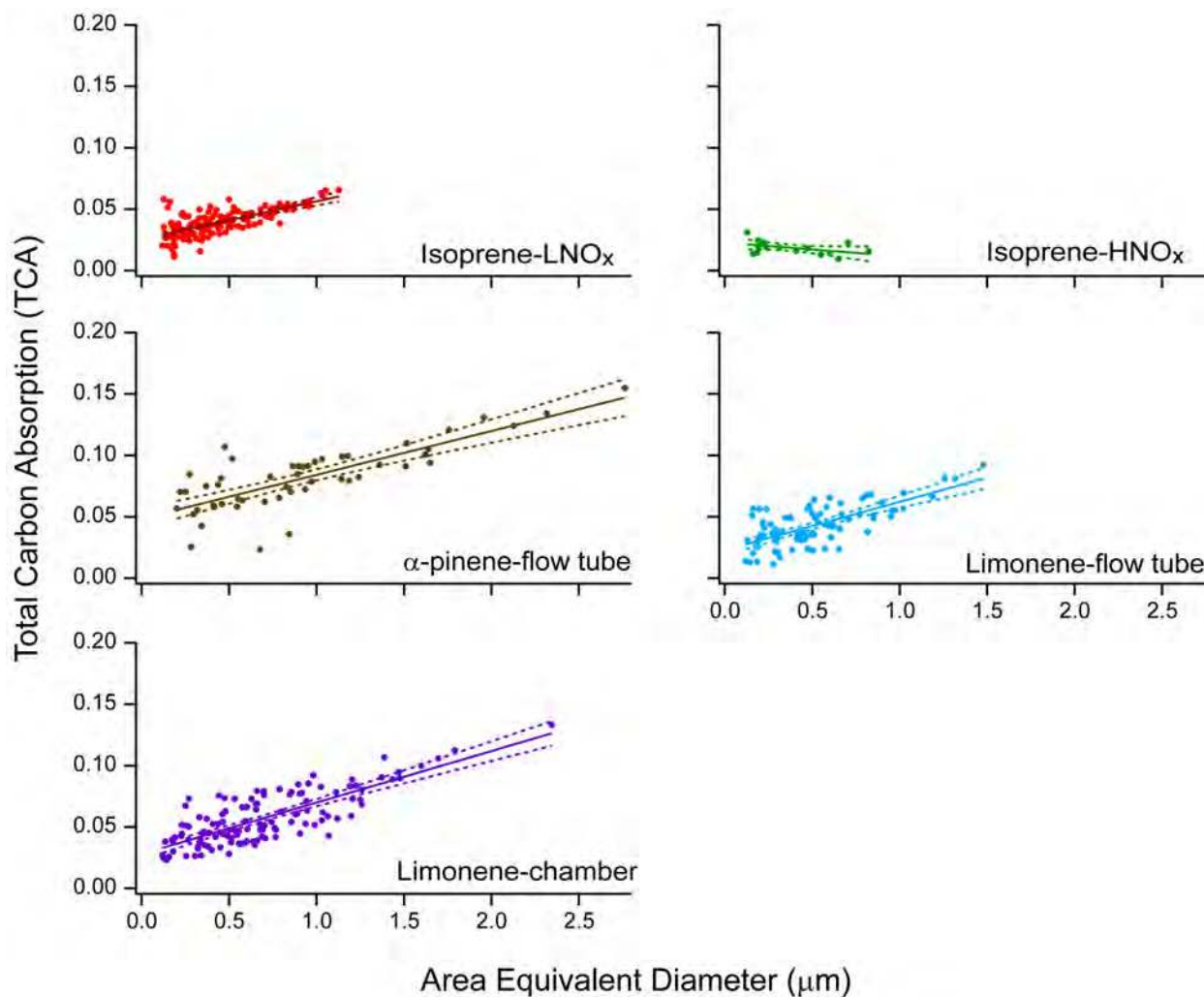
126

127

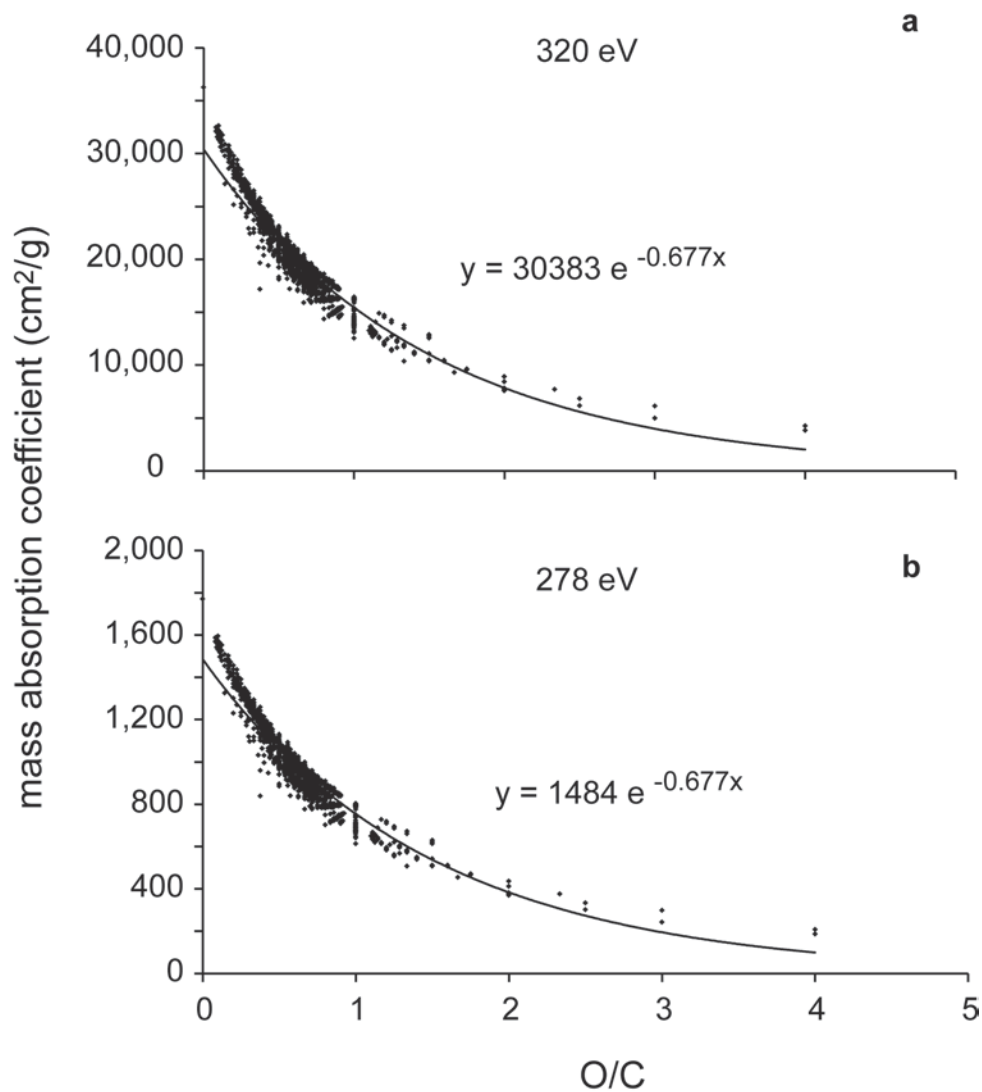
128 **Figure S1.** Optical thickness of carbon (total carbon absorption =  $OD_{320}-OD_{278}$ ) as a function of  
129 size of impacted organic particles for each ambient data set. Solid lines are best fit lines for each  
130 data set and dashed lines are  $\pm 95\%$  confidence intervals. The thick fitted lines are reproduced in  
131 Figure 2 of the main text, and the slopes, intercepts, and confidence intervals are listed in Table  
132 1.

133

134



135  
 136  
 137 **Figure S2.** Optical thickness of carbon (total carbon absorption =  $\text{OD}_{320} - \text{OD}_{278}$ ) as a function of  
 138 size of impacted organic particles for each laboratory data set. Solid lines are best fit lines for  
 139 each data set; the same lines are reproduced in Figure 2 of the main text. The slopes are listed in  
 140 Table 1.  
 141  
 142



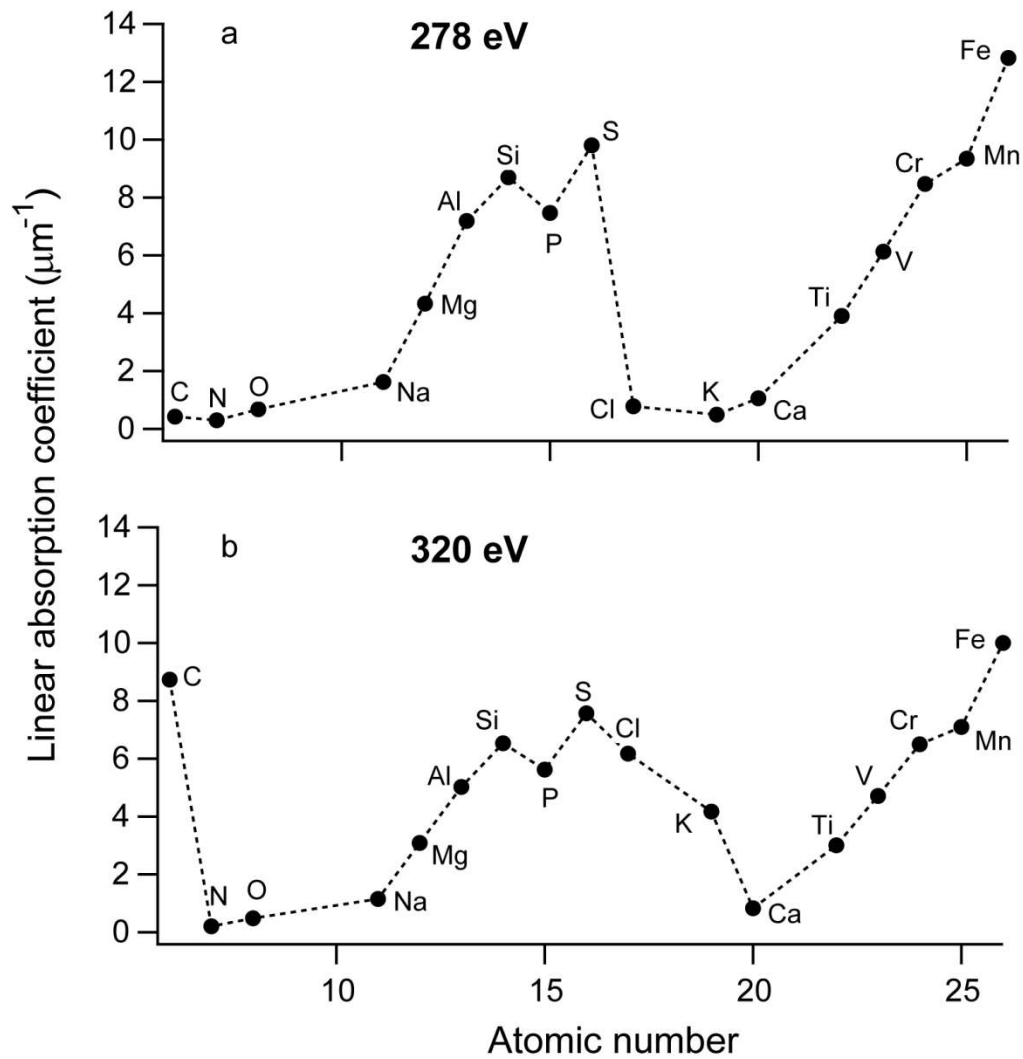
143

144 **Figure S3.** Calculated mass absorption coefficients as a function of O/C at a) 320 eV and b) 278

145 eV for chemical formulas from organic molecules found in atmospheric aerosols.

146

147



148  
 149 **Figure S4.** Linear absorption coefficients at (a) 278 eV and (b) 320 eV for elements found in  
 150 atmospheric aerosols [Henke *et al.*, 1993].

151  
 152  
 153  
 154  
 155  
 156

157 **Table S1.** Ambient sample collection information and fitting results for OD<sub>320</sub> and OD<sub>278</sub> vs. area  
 158 equivalent diameter.<sup>a</sup>

Campaign	Year	Number of particles	320 eV		278 eV	
			Slope	Intercept	Slope	Intercept
CARES	2010	2428	0.14±0.005	0.024±0.003	0.045±0.002	0.016±0.001
MILAGRO	2006	798	0.13±0.01	0.048±0.005	0.057±0.005	0.019±0.002
NAOPEX	2001	123	0.15±0.02	0.028±0.01	0.069±0.007	0.008±0.006
VOCALS	2008	125	0.20±0.04	0.042±0.02	0.098±0.02	0.023±0.01
YACS	2002	56	0.14±0.02	0.029±0.01	0.027±0.01	0.025±0.006

159 <sup>a</sup>The ±95% confidence intervals for the slope and intercept are given.

160  
 161  
 162  
 163  
 164  
 165  
 166  
 167  
 168  
 169  
 170  
 171  
 172

173 **Table S2.** Laboratory sample fitting results for total carbon absorption (TCA) vs. area  
 174 equivalent diameter.<sup>a</sup>

Sample	MOUDI stage	Number of particles	Slope	Intercept	R <sup>2</sup>
Isoprene-LNOx	7	137	0.031±0.006	0.025±0.003	0.48
Isoprene-HNOx	7	16	-0.011±0.01	0.023±0.005	0.22
α-pinene-flow tube	7	51	0.036±0.008	0.048±0.009	0.63
Limonene-flow tube	7	87	0.039±0.009	0.023±0.005	0.49
Limonene-chamber	8	122	0.042±0.006	0.028±0.005	0.62

175 <sup>a</sup>The ±95% confidence intervals for the slope and intercept are given. LNOx and HNOx refer to  
 176 low-NOx and high-NOx oxidation by OH; ozone is used as the oxidant for the remaining  
 177 samples.

178  
 179  
 180  
 181  
 182  
 183  
 184  
 185  
 186  
 187  
 188  
 189

190 **Table S3.** Laboratory sample fitting results for OD<sub>320</sub> and OD<sub>287</sub> vs. area equivalent diameter.<sup>a</sup>

Sample	320 eV		278 eV	
	Slope	Intercept	Slope	Intercept
Isoprene-LNO <sub>x</sub>	0.039±0.004	0.040±0.002	0.0083±0.002	0.014±0.001
Isoprene-HNO <sub>x</sub>	0.0036±0.009	0.033±0.004	0.015±0.007	0.011±0.003
α-pinene-flow tube	0.040±0.008	0.063±0.009	0.0042±0.001	0.015±0.001
Limonene-flow tube	0.042±0.008	0.037±0.005	0.0027±0.002	0.014±0.001
Limonene-chamber	0.047±0.006	0.043±0.005	0.0049±0.002	0.015±0.001

191

192 <sup>a</sup>The ±95% confidence intervals for the slope and intercept are given. LNO<sub>x</sub> and HNO<sub>x</sub> refer to  
 193 low-NO<sub>x</sub> and high-NO<sub>x</sub> oxidation by OH; ozone is used as the oxidant for the remaining  
 194 samples.

195

196

197

198

199

200

201

202

203

204

205

206



207 **Table S4.** Summary of experimental conditions for the chamber experiments<sup>a</sup>

Sample	[HC]	Oxidant	[NO]	[NO <sub>y</sub> ]	[O <sub>3</sub> ]	T	Concentration	Average
	ppm	precursor	ppb	ppb	ppb	(°C)	(μg/m <sup>3</sup> )	Size (nm)
Isoprene-LNOx	1.0	H <sub>2</sub> O <sub>2</sub>	<1	5	3	25	40.8	326
Isoprene-HNOx	1.1	H <sub>2</sub> O <sub>2</sub>	430	530	4	24	192	174
Limonene <sup>b</sup>	0.30	Ozone	<1	6	590	24	1251	177

208 <sup>a</sup>The [HC] are the initial mixing ratios after injection of the liquid precursor, the remaining  
 209 values were measured at the start of the sample collection.

210 <sup>b</sup>The Limonene chamber experiment was done in the dark.

211

212

213

214

215

216

217

218

219

220

221

222

223

224

225

226

227 **Table S5.** Average organic to inorganic thickness ratios for each campaign.

Campaign	$d_{org}/d_{in}$ (% of thickness that is inorganic)		
	In = S, metals etc	In=NaCl	In=(NH <sub>4</sub> ) <sub>2</sub> SO <sub>4</sub>
CARES	6.7 (13%)	5.5 (15%)	2.2 (31%)
MILAGRO	7.8 (11%)	6.4 (13%)	2.6 (28%)
NAOPEX	7.2 (12%)	5.9 (14%)	2.4 (30%)
VOCALS	3.6 (22%)	2.9 (26%)	1.1 (47%)
YACS	7.7 (12%)	6.3 (14%)	2.5 (28%)

228

229

230

231

232

233

234

235

236

237

238

239

240

241

242